Research Article | Vol. 9, No. 12 | 1 Dec 2018 | BIOMEDICAL OPTICS EXPRESS 6331
Biomedical Optics EXPRESS

Clinical feasibility of optical coherence micro-elastography for imaging tumor margins in breast-conserving surgery

Wes M. Allen,[1,2,*] Ken Y. Foo,[1,2] Renate Zilkens,[1,3] Kelsey M. Kennedy,[1,2,4] Qi Fang,[1,2] Lixin Chin,[1,2] Benjamin F. Dessauvagie,[5,6] Bruce Latham,[5] Christobel M. Saunders,[3,7,8] and Brendan F. Kennedy[1,2]

[1]*BRITElab, Harry Perkins Institute of Medical Research, QEII Medical Centre, Nedlands and Centre for Medical Research, The University of Western Australia, Perth, Western Australia, 6009, Australia*
[2]*Department of Electrical, Electronic & Computer Engineering, School of Engineering, The University of Western Australia, 35 Stirling Highway, Perth, Western Australia, 6009, Australia*
[3]*Division of Surgery, Medical School, The University of Western Australia, 35 Stirling Highway, Perth, Western Australia, 6009, Australia*
[4]*Current address: Department of Biomedical Engineering, Columbia University, 622 W 168th St, New York, NY 10025, USA*
[5]*PathWest, Fiona Stanley Hospital, 11 Robin Warren Drive, Murdoch, Western Australia, 6150, Australia*
[6]*Division of Pathology and Laboratory Medicine, Medical School, The University of Western Australia, 35 Stirling Highway, Perth, Western Australia, 6009, Australia*
[7]*Breast Centre, Fiona Stanley Hospital, 11 Robin Warren Drive, Murdoch, Western Australia, 6150, Australia*
[8]*Breast Clinic, Royal Perth Hospital, 197 Wellington Street, Perth, Western Australia, 6000, Australia*
**wes.allen@research.uwa.edu.au*

Abstract: It has been demonstrated that optical coherence micro-elastography (OCME) provides additional contrast of tumor compared to optical coherence tomography (OCT) alone. Previous studies, however, have predominantly been performed on mastectomy specimens. Such specimens typically differ substantially in composition and geometry from the more clinically relevant wide-local excision (WLE) specimens excised during breast-conserving surgery. As a result, it remains unclear if the mechanical contrast observed is maintained in WLE specimens. In this manuscript, we begin to address this issue by performing a feasibility study of OCME on 17 freshly excised, intact WLE specimens. In addition, we present two developments required to sustain the progression of OCME towards intraoperative deployment. First, to enable the rapid visualization of *en face* images required for intraoperative assessment, we describe an automated segmentation algorithm to fuse *en face* micro-elastograms with OCT images to provide dual contrast images. Secondly, to validate contrast in micro-elastograms, we present a method that enables co-registration of *en face* images with histology of WLE specimens, sectioned in the orthogonal plane, without any modification to the standard clinical workflow. We present a summary of the observations across the 17 specimens imaged in addition to representative micro-elastograms and OCT images demonstrating contrast in a number of tumor margins, including those involved by invasive ductal carcinoma, mucinous carcinoma, and solid-papillary carcinoma. The results presented here demonstrate the potential of OCME for imaging tumor margins.

© 2018 Optical Society of America under the terms of the OSA Open Access Publishing Agreement.

1. Introduction

Wide-local excision (WLE) is the standard procedure for removal of malignant tumors during breast-conserving surgery [1]. During WLE, the surgeon aims to remove the entire tumor

#342473 https://doi.org/10.1364/BOE.9.006331
Journal © 2018 Received 21 Aug 2018; revised 26 Oct 2018; accepted 8 Nov 2018; published 19 Nov 2018

Biomedical Optics EXPRESS

surrounded by a rim of normal tissue, referred to as the surgical margin. However, 20–30% of patients require additional surgery because tumor is found within the surgical margin, an involved margin, which is associated with a higher rate of recurrence [2–5]. A key reason for these high re-excision rates is that, currently, the status of the margins is not known until the post-operative histopathological analysis is performed days later on the excised tissue [6,7]. A number of techniques have been developed for intraoperative margin assessment [8,9]. The most commonly used intraoperative margin assessment technique is frozen section analysis, where the specimen is serially sectioned, rapidly frozen, sectioned in a cryostat, fixed and assessed by a pathologist [8,10]. However, there are significant disadvantages that limit the effectiveness of frozen section analysis, for example, personnel resourcing [8], and damage to the specimen during the freezing process, which can result in low-quality histology slides [11].

An array of emerging techniques have been proposed to improve on those in current use [12–23]. One group of techniques, which includes confocal microscopy [12,19], fluorescence imaging [24], light sheet microscopy [14], Cerenkov luminescence imaging [25] and nonlinear microscopy [20,21], require exogenous contrast agents. These agents can be applied to the surface of the excised specimen or, in some cases, injected intravenously before surgery [25]. While these techniques hold great promise and generate images with cellular resolution that can be evaluated analogously to histology, the use of such agents adds to their complexity, and there is significant value in pursuing label-free techniques [26]. Label-free techniques rely on endogenous contrast, for example, optical scattering or mechanical properties, for visualizing tumor [26]. While these techniques typically cannot provide molecular-level contrast, the relative simplicity of imaging endogenous contrast facilitates rapid structural imaging. Among the label-free techniques, optical coherence micro-elastography (OCME), a variant of optical coherence elastography [27,28], has shown promise for the visualization of tumor in human breast tissue [29–31].

OCME generates mechanical contrast by mapping micro-scale deformation (local axial strain) resulting from a quasi-static compressive load [32]. As OCME utilizes phase-sensitive optical coherence tomography (OCT) to measure local strain, the opportunity exists to generate images with combined mechanical and optical contrast. This approach provides complementary contrast that enhances visualization of features in human breast tissue over OCT alone. For example, local strain often provides higher contrast than OCT in differentiating turbid tissues, such as stroma, fibroglandular tissue, and invasive tumor [30,31,33]. On the other hand, OCT readily delineates adipose tissue, manifesting as a distinctive honeycomb structure, whilst local strain is erratic in adipose tissue due to the hyposcattering spherical fat reservoirs [32,33].

To take advantage of this dual contrast, fused images, known as micro-elastograms, are generated by first segmenting OCT images into dense tissue and non-dense tissue, then overlaying the measured local strain on regions of dense tissue only and presenting the OCT intensity in regions of non-dense tissue [30,31]. To facilitate rapid assessment across a wide-field-of-view (up to ~46 × 46 mm) micro-elastograms (and OCT images) are presented in the *en face* plane. *En face* visualization also takes advantage of the high lateral resolution of the OCT system, as estimating axial strain results in an effective degradation of the axial resolution (compared to OCT images) while the lateral resolution is maintained [30,32]. Previous work has demonstrated that fused micro-elastograms can increase contrast over OCT images in a range of features in human breast tissue, including invasive tumor, *in situ* tumor, ducts, and blood vessels [29–31,33].

A primary issue with previous studies, however, is that, except for one WLE specimen [31], they have been predominantly performed on specimens dissected from the central tumor mass of mastectomies. Imaging mastectomy specimens demonstrated the capability of OCME to visualize tumor and enabled histology to be presented in the same plane as *en face* images, thus providing direct validation [29–31]. However, mastectomy specimens often contained

Biomedical Optics EXPRESS

dense, macro-scale regions of advanced tumor, typically extending through the specimen. In the more clinically relevant scenario of imaging tumor margins in WLE specimens, only the leading edge of the tumor mass, often comprising small tendrils of the tumor surrounded by adipose tissue, are expected to be present at the surgical margin. Furthermore, mastectomy specimens are imaged following serial sectioning, or bread-loafing, and they are typically flatter and thinner than WLE specimens. As the tissue boundary can have a significant impact on micro-elastogram quality, the surface unevenness present in WLE specimens may adversely affect contrast in micro-elastograms [30,34]. The increased sample thickness in WLE specimens also necessitates the application of larger compression to ensure sufficient strain signal-to-noise ratio to generate high-quality micro-elastograms [35]. As such, while previous mastectomy studies have validated the potential of OCME for visualization of tumor, and the WLE specimen presented previously provided proof-of-principle [31], it is not clear if OCME will be suited for visualizing a range of tumor morphologies in a large set of WLE specimens.

In this manuscript, we present a study investigating the clinical feasibility of OCME for imaging tumor margins of WLE specimens. We perform OCME on 28 margins from 17 freshly excised specimens from patients undergoing breast-conserving surgery. We present a summary of observations of common tissue types present in the tumor margins imaged during the study. The representative micro-elastograms and OCT images presented in this manuscript demonstrate the capability of OCME to identify a range of features, including invasive ductal carcinoma, mucinous carcinoma, and solid-papillary carcinoma. In addition, we present an automated algorithm that fuses strain with OCT images by segmenting the OCT images into dense and non-dense tissue regions to generate micro-elastograms, previously performed manually. To enable validation of the contrast obtained, accurate co-registration of gold-standard histology with wide-field *en face* images is required. We present a new method to achieve this for WLE specimens, which, unlike mastectomy specimens, are sectioned in the plane orthogonal to *en face* images; importantly, this method does not require any modification to the standard clinical workflow. The results presented here demonstrate the clinical feasibility of OCME for imaging tumor margins in breast-conserving surgery and highlight the complementary contrast provided by analysis of micro-elastograms alongside OCT images.

2. Materials and methods

2.1 OCME system

The OCME system comprises three main components: the OCT system, the specimen mounting mechanism and the wide-field translation system. The OCT system is based on a Telesto II spectral-domain system (TEL220C1, Thorlabs Inc., USA). The measured full-width-at-half-maximum axial and lateral resolutions are 5.5 μm and 13 μm in air, respectively. The measured displacement sensitivity of the OCT system is 1.4 nm at an OCT signal-to-noise ratio of 40 dB, acquired under clinical testing conditions [34].

The tissue mounting mechanism comprises a motorized laboratory jack, a piezoelectric actuator, and an imaging window. The laboratory jack (MLJ050/M, Thorlabs Inc., USA) applies a preload strain to the specimen, ensuring sufficient contact between the imaging window and the specimen. The piezoelectric actuator (Piezomechanik GmbH, Germany) applies quasi-static compression to the tissue (described in Section 2.2) and has an aperture of 65 mm and a maximum stroke of 9.5 μm. The 75-mm diameter imaging window (84-359, Edmund Optics Inc., USA), fixed to the piezoelectric actuator, transfers the compressive load from the actuator to the specimen. The OCT system is configured in common-path mode, with the interface between the imaging window and the tissue acting as the reference reflector [29].

The wide-field translation system moves the entire tissue mounting mechanism relative to the OCT scan head to generate wide-field images (~46 × 46 mm). The translation stages

Biomedical Optics EXPRESS

(NRT100/M, Thorlabs Inc., USA) have a range of 100 mm and accelerate at 30 mm s^{-2} to a maximum velocity of 30 mm s^{-1}. Wide-field images are generated by acquiring individual OCT volumes (termed sub-volumes) and performing a mosaicking technique in post-processing, as described previously [31,34].

2.2 Acquisition and post-processing protocol

Individual sub-volumes (measuring 16 × 16 × 3.5 mm) are acquired with 808 A-scans per B-scan and 2,424 B-scan pairs. The A-scan rate used in this study is ~71 kHz. Each B-scan pair comprises two B-scans acquired at different compression levels in the same spatial location, every 6.6 μm in the *y*-plane [29]. During post-processing, the phase-difference is calculated between B-scans in a pair via the Kasai phase estimator and three phase-difference B-scans are averaged together [29,36]. The axial displacement at each lateral and axial location in a sub-volume is calculated from the phase difference. The local axial strain, defined as the gradient of the displacement with respect to depth, is estimated at each spatial location using weighted least squares linear regression, over a fitting range of 100 μm [32]. The fitting range results in an effective degradation in strain resolution in the axial plane, meaning it is lower than the OCT axial resolution [30]. Presenting *en face* micro-elastograms for clinical interpretation capitalizes on the maintenance of high lateral resolution, in addition to enabling rapid assessment of tissue across wide field-of-views [31,32].

Wide-field *en face* images are generated by mosaicking *en face* sub-images. The technique overlaps sub-images by 1 mm in the *en face* plane, to ensure accurate alignment is achieved and to minimize areas of low OCT intensity due to coherence gate curvature [31,34]. Wide-field *en face* micro-elastograms are generated by presenting strain (in a perceptually linear colormap [37]) in regions of dense tissue only, fused with grayscale OCT images, using a custom segmentation algorithm (described in Section 2.3). Wide-field *en face* OCT images are presented in grayscale on a logarithmic scale. The depth (optical path length) of *en face* images is indicated in each image in Section 3.

2.3 Segmentation algorithm

To automate the generation of fused *en face* micro-elastograms, an algorithm was developed to segment the wide-field OCT scans into dense and non-dense tissue regions. The input to this algorithm is a wide-field *en face* OCT image, and the output is a binary mask labeling dense tissue regions with one and non-dense tissue regions with zero. The mask is used to produce fused micro-elastograms in which strain is presented in dense tissue regions, and OCT is presented in non-dense tissue regions. This algorithm comprises four stages: filtering, in which noise is removed from the image; binarization, in which a binary image is produced via intensity thresholding; area thresholding, in which small components in the binary image are removed; and clean-up, in which small holes in the binary mask are closed. Figure 1 shows a flowchart summarizing this algorithm.

A representative 'unfused' image of local axial strain is shown in Fig. 1(a) and the corresponding OCT image (the algorithm input) is shown in Fig. 1(b). During the filtering stage, Fig. 1(c), the noise reduction of the OCT image is achieved using anisotropic diffusion [38], followed by hybrid median filtering [39]. Anisotropic diffusion smooths the image to reduce noise, without significantly degrading edge contrast [38]. A 3 × 3 pixel hybrid median filter is then used to remove single pixel 'salt and pepper' noise. Compared to a standard median filter, hybrid median filtering better preserves edges and corners [39]. As dense tissue is typically more highly scattering than non-dense tissue, signal intensity thresholding (using a global Otsu threshold [40]) is used to create a preliminary dense tissue mask (Fig. 1(d)).

Regions of adipose cell membranes were then masked out by calculating the areas of connected components in the binary image, and thresholding to filter out components with an area less than 200 $pixels^2$ (78,408 μm^2, Fig. 1(e)). This value was tuned by testing the binary algorithm on multiple (>10) wide-field OCT images. Since the hyperscattering membranes

Biomedical Optics EXPRESS

surrounding adipose cells are typically much smaller than dense tissue regions, filtering binary components with small surface area allows adipose cell membranes to be removed from the segmentation mask. Finally, morphological closing was applied to fill in small holes in dense tissue regions created by residual noise (Fig. 1(f)). The resulting binary mask, Fig. 1 (g), was then used to produce fused micro-elastograms (Fig. 1(h)). The accuracy of the algorithm was assessed qualitatively by comparing the resulting fused *en face* micro-elastogram with corresponding OCT images. The use of the algorithm has reduced the time required to generate a single wide-field *en face* micro-elastogram from ~30 minutes using the manual method described previously [31] to ~20–30 seconds, a critical step to enable future intraoperative deployment of OCME.

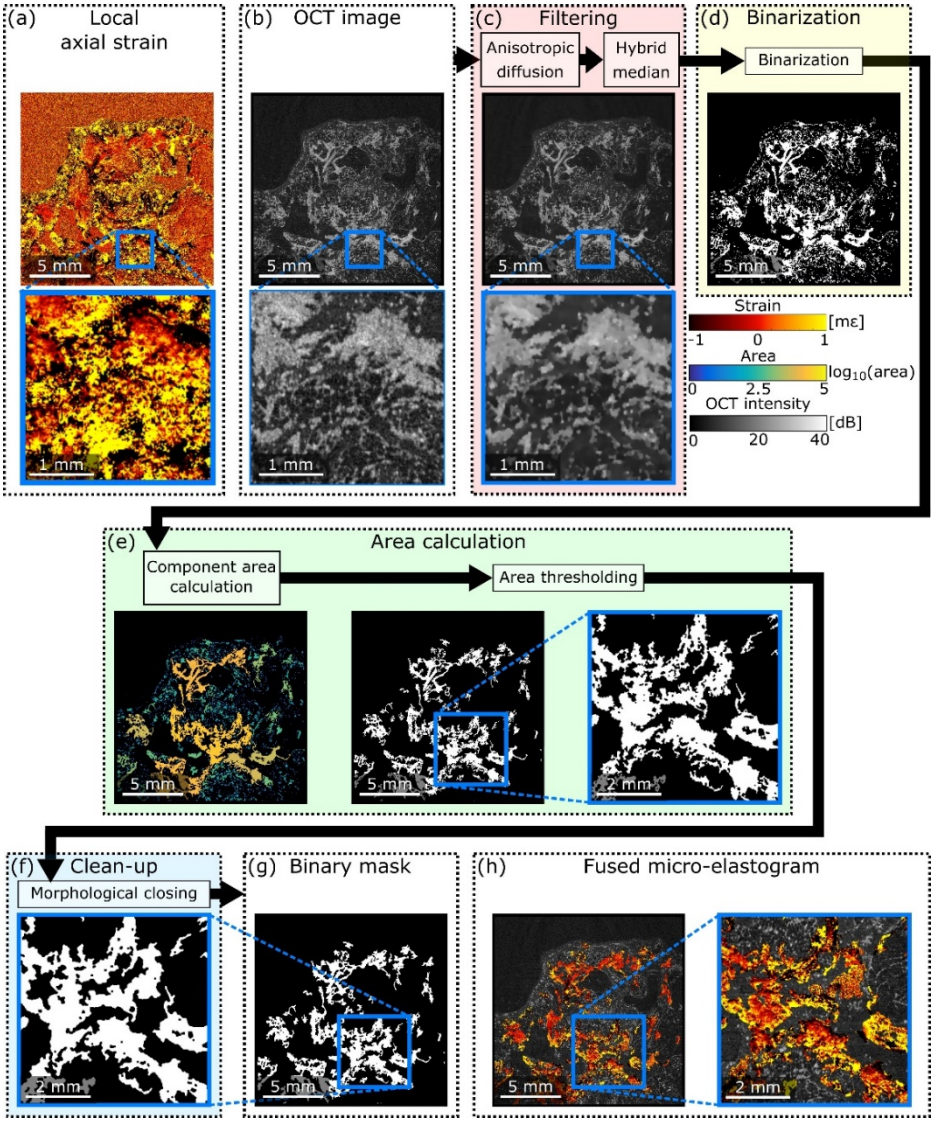

Fig. 1. Flowchart for the segmentation algorithm. (a) *En face* local axial strain image. (b) Input *en face* OCT image. (c) Filtering stage. (d) Binarization stage. (e) Area thresholding stage. (f) Clean-up stage. (g) Segmentation mask. (h) Fused micro-elastogram.

Biomedical Optics EXPRESS

2.4 Clinical protocol

WLE specimens were obtained from patients undergoing breast-conserving surgery at Fiona Stanley Hospital, Western Australia (Project No: FSH-2015-032). Informed consent was obtained from patients, and the ethics for this research project has been approved by the Sir Charles Gairdner and Osborne Park Health Care Group Human Research Ethics Committee (HREC No: 2007-152). In this study, 28 margins were imaged from 17 WLE specimens. Following surgery, fresh specimens were transferred from the operating theater to the anatomical pathology laboratory where they were inspected and checked in following standard protocols before scanning. For each specimen, up to two margins were scanned within 30 minutes from when the research team received the specimen. Each wide-field OCME data set took ~10 minutes to acquire using the scanning parameters outlined in Section 2.2. In cases where two margins were scanned, following the first scan, the specimen was removed from the loading mechanism, rotated to the new orientation, photographed before being placed back on the loading mechanism and the second scan performed. OCME scanning was performed between ~1–2 hours after excision.

The specimen's orientation was indicated by the placement of sutures and clips during surgery, visible in Fig. 2(a). During OCME scanning, the orientation of the specimens was recorded for later co-registration of histology slides, described in Section 2.5. Following scanning, specimens were inked for orientation in histopathology and fixed in 10% neutral-buffered formalin for at least 24 hours. The specimens were typically serially sectioned perpendicular to the medial-lateral plane following standard protocols (however, the specimen in Fig. 2 was sectioned perpendicular to the inferior-superior plane). Cross-sections were taken of the first and last slices of the specimen, *e.g.*, A1 in Fig. 2(a). Sections of the tumor, close-by margins and other areas of interest were sampled and placed in cassettes for histopathology processing. These cassettes were processed into paraffin blocks, one section, ~4 μm thick, from each block was mounted on glass slides and stained with hematoxylin and eosin. The glass slides were scanned at 40 × magnification to generate digital micrographs for subsequent analysis by a pathologist. The pathology handling process is documented in the pathology report, following standard protocols.

2.5 Histology co-registration and validation

Accurate co-registration of digital micrographs with wide-field *en face* images is required to validate contrast obtained from OCME measurements. Imaging mastectomy specimens in previous studies enabled digital micrographs to be presented in the same plane as *en face* images, providing direct validation of contrast. However, the standard clinical workflow for preparing histology slides of WLE specimens, described in Section 2.4, results in digital micrographs in the plane orthogonal to *en face* images. In this section, we describe a method developed to co-register digital micrographs with wide-field *en face* images that requires no additional modification to the standard clinical workflow or documentation.

A schematic illustrating this process is shown in Fig. 2(a). The orientation and dimensions of the whole specimen are recorded by photographing the specimen on a calibration grid before OCME scanning. For each specimen, the research team obtains the following information from the sectioned specimen key and the final pathology report: inking details, dimensions of the specimen after chemical fixation, and pathology handling information such as the numbering of the tissue slices and cassettes. The thickness of the first and last slices is 10 mm unless otherwise documented in the pathology report. The thickness of the remaining slices is estimated by subtracting the thickness of the first and last slice from the overall length of the fixed specimen and dividing this by the number of tissue slices. A correction factor for shrinkage is calculated by dividing the length before fixation by the length after fixation. The thickness of the tissue slices is multiplied by the correction factor. The location

Biomedical Optics EXPRESS

of digital micrographs is approximated, to within the thickness of the tissue slice (~3–7 mm in our experience), and indicated on the *en face* OCT image.

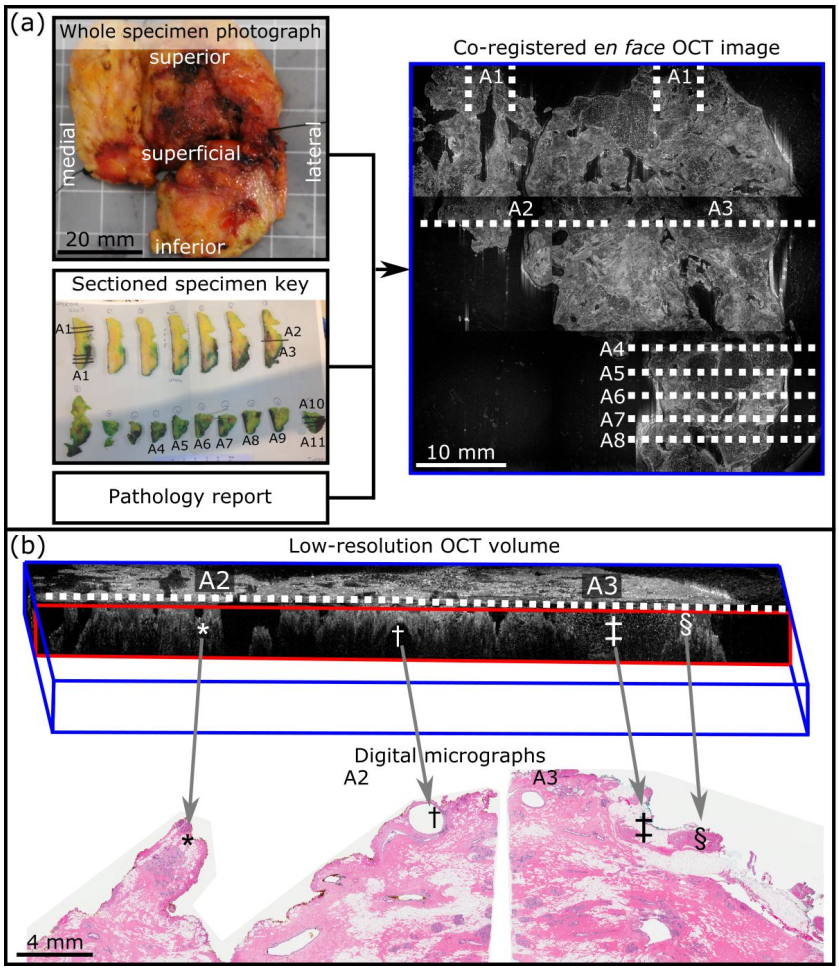

Fig. 2. Histology co-registration and validation process. (a) Schematic outlining the process to estimate the location of tissue slices on the *en face* OCT image. (b) Validation of co-registration using low-resolution OCT volume to match digital micrographs. *, †, ‡, and § indicate co-registered features; *, change in surface topology; †, apocrine cyst; ‡, adipose tissue; § dense tissue.

To validate the positioning of the digital micrographs, sequences (or stacks) of *en face* wide-field OCT images, at intervals of 20 µm and up to a depth of 1 mm, are loaded into image processing software, and assembled into low-resolution wide-field OCT volumes, Fig. 2(b), using the Volume Viewer plugin for ImageJ software (ImageJ/Fiji, v1.51w) [41]. The OCT volume is sliced in the cross-sectional plane in the expected location of the digital micrograph. Features such as clusters of adipose cells, strands of dense tissue or gross changes in surface topology, are identified from cross-sectional views extracted from the low-resolution OCT volume and corresponding digital micrographs (Fig. 2(b)). In cases where the OCT cross-section does not match the first approximation of the digital micrograph location, the position of the cross-sectional view within the OCT volume is adjusted to determine the exact location and the new positioning of the digital micrograph updated on the *en face* image. A mismatch typically occurs as it is not standard practice to record which face of the tissue slice is placed facing upwards in the cassette and therefore, sectioned for

Biomedical Optics EXPRESS

staining. As a result, the 4 µm thick section could be produced from either face of the tissue slice. However, in a given specimen, the face of the tissue slice sectioned is typically consistent. Therefore, the assumed distance between digital micrographs is not affected. The histology matching was performed by the research team and was evaluated and confirmed against *en face* images by a pathologist. The representative results presented in Section 3 demonstrate the accuracy of the technique across a range of specimens. Once matching was confirmed to be accurate, *en face* images and digital micrographs were then annotated with a pathologist to identify features in the margin. Tumor detected in the margin, defined here as <1 mm from the edge of the specimen, as is common with other emerging techniques [13,42], is referred to here as an involved margin.

3. Results

OCME was performed on 28 margins from 17 WLE specimens. From the pathology reports, ten specimens contained invasive tumors only, four contained a mix of invasive and *in situ* tumors, and three contained *in situ* tumors only. Five of the imaged margins contained tumor <1 mm from the edge of the specimen, *i.e.*, involved margins. The remaining 23 margins were mainly comprised of adipose tissue and stroma. Other features that were identified included ducts, terminal duct lobular units, and blood vessels. Two of the involved margins, both from the same specimen, contained invasive ductal carcinoma; the remaining involved margins contained solid papillary carcinoma, mucinous carcinoma, and lobular carcinoma. None of the involved margins contained *in situ* tumor. In four of the involved margins, the tumor was confidently identified in the micro-elastograms and OCT images during image analysis by the research team. In the last case, the tumor was situated ~800 µm from the edge of the tissue in the digital micrograph. While a region of dense tissue was visible in this area, in this case, the strain and OCT intensity had degraded too much at this depth to confidently detect the tumor. Table 1 provides a summary of the most common tissue types identified in the margins imaged in this study. For most tissue types, fused micro-elastograms were found to provide additional contrast in visualizing tissue types in the margins imaged over the OCT image. However, in some cases, *e.g.*, adipose tissue and mucinous carcinoma, the OCT image provided greater contrast. The summary in Table 1 highlights the complementary contrast provided by analyzing fused micro-elastograms alongside OCT images.

In the following section, representative *en face* micro-elastograms and OCT images of four surgical margins are presented. These results demonstrate the potential for OCME to visualize involved margins by showing contrast for a range of features, including invasive ductal carcinoma, mucinous carcinoma, and solid-papillary carcinoma. Although the number of involved margins imaged throughout this study allows OCME to be assessed qualitatively, significantly more work is required to obtain a sufficient number of images for quantitative analysis to be meaningful; therefore, this is not provided here. The representative results presented also highlight some obstacles that must be overcome to further progress OCME to clinical translation, for example, subtle strain patterns in highly cellular invasive tumor, thermal damage due to the use of electrosurgical instruments and non-contact between the imaging window and specimen. For each of the representative result, we present an annotated digital micrograph with co-registered B-scans and a video fly-through of magnified *en face* images from a depth of 20 µm to 1 mm which allow the entire 1 mm margin to be assessed. High-resolution digital micrographs are provided in Visualization 1. As the system is configured in common-path mode [29], the top of the B-scan corresponds to the imaging window-specimen interface. The automated segmentation algorithm has been optimized for the *en face* view, therefore, fused micro-elastogram B-scans were generated using manual segmentation, described previously [31].

Figure 3 contains images of uninvolved stroma acquired from the lateral margin of a WLE specimen excised from a 67-year-old patient. This result demonstrates that the characteristic homogeneous strain in uninvolved stroma, observed in mastectomy specimens, is retained in

Biomedical Optics EXPRESS

WLE specimens [30]. A photograph of the margin, which measured 50 × 65 mm, is shown in Fig. 3(a). Three clips (C) are visible in Fig. 3, identifying this surface as the lateral margin. Analysis of the digital micrograph, Fig. 3(b), revealed the specimen contained uninvolved stroma (S) and adipose tissue (A). Co-registered B-scans are presented in Fig. 3(b). The location of the digital micrograph in *en face* images is indicated by the white dashed lines in Fig. 3(c)-3(f). The wide-field micro-elastogram, Fig. 3(c), shows the specimen contains a mix of adipose tissue and dense tissue. The strain appears mostly uniform, indicative of uninvolved stroma [30]. The magnified micro-elastogram, Fig. 3(d), shows the uniform strain in more detail. A large region of non-contact (NC) is visible in the magnified micro-elastogram. The magnified OCT image, Fig. 3(f), shows the dense tissue exhibits mostly uniform OCT intensity, indicative of uninvolved stroma [33]. However, an area of heterogeneous OCT intensity, indicated by the arrow in Fig. 3(f), could be misinterpreted as invasive tumor. These images demonstrate the benefit of the mechanical contrast provided by micro-elastograms compared to OCT images alone in analyzing tumor margins.

Table 1. Summary of observations of common tissue types present in the margins imaged during the study.

Tissue type	OCT image contrast	Fused micro-elastogram contrast
Adipose tissue	Distinctive honeycomb structure.	Relies on OCT contrast, as strain is not displayed in adipose tissue following segmentation.
Stroma - thin connective strands	Well-organized, trabecular pattern.	Typically appears as well-organized, trabecular pattern. Strain accentuates the trabecular structure compared to OCT. In some cases, can appear heterogeneous due to underlying adipose tissue.
Stroma - solid mass	Homogeneous or well-organized dense region, often transitions to adipose tissue deeper into the scan.	Strain is typically smooth, or a well-organized, trabecular pattern. However, in some cases can manifest as heterogeneous if excessive thermal damage, micro-scale non-contact present, or due to boundary effects where adipose tissue is infiltration stroma.
Ducts	Appears as circular or tubular structures with hyperscattering walls. Can appear 'full' (interior has slightly lower scattering than the wall), or 'empty' (hyposcattering interior). Ducts imaged in this study were typically 0.1-1 mm in diameter.	Strain typically appears as a crater-like or tubular structure with an abrupt change from positive to negative strain at the boundary of the duct. Strain accentuates the boundaries of duct compared to OCT.
Terminal duct lobular unit	Appears as 'grape-like' structure in OCT, however, contrast is often subtle.	Appears as distinctive 'grape-like' structures. Strain accentuates the lobular unit compared to OCT.
Vessel	Vessels typically have well-delineated hyperscattering walls and often appear 'empty' inside.	Appears as a crater or tubular structure, similar to a duct. Strain accentuates the boundaries of vessel compared to OCT.
Highly-cellular invasive ductal carcinoma[a,b]	Heterogeneous OCT intensity, however, the contrast is subtle.	Heterogeneous texture in strain, however, the contrast is subtle.
Invasive lobular carcinoma[a,b]	Heterogeneous OCT intensity	Heterogeneous strain pattern
Mucinous carcinoma[a,b]	Appears as more uniformly scattering 'pools' of mucin, distinct from adipose tissue.	Strain is displayed in adipose tissue following segmentation, however, contrast primarily from the OCT image
Solid papillary carcinoma[a,b]	Interior of carcinoma displays lower OCT intensity, however, the contrast is subtle.	Appears as a crater structure, similar to a duct, however with a larger diameter and is nodular. Strain accentuates the boundaries.

[a]Observations for these carcinomas are based on the one example of each imaged during this study. [b]A common trait of all carcinomas imaged that they remained present, or grew in size, deeper within the specimen and did not transition to adipose tissue.

Biomedical Optics EXPRESS

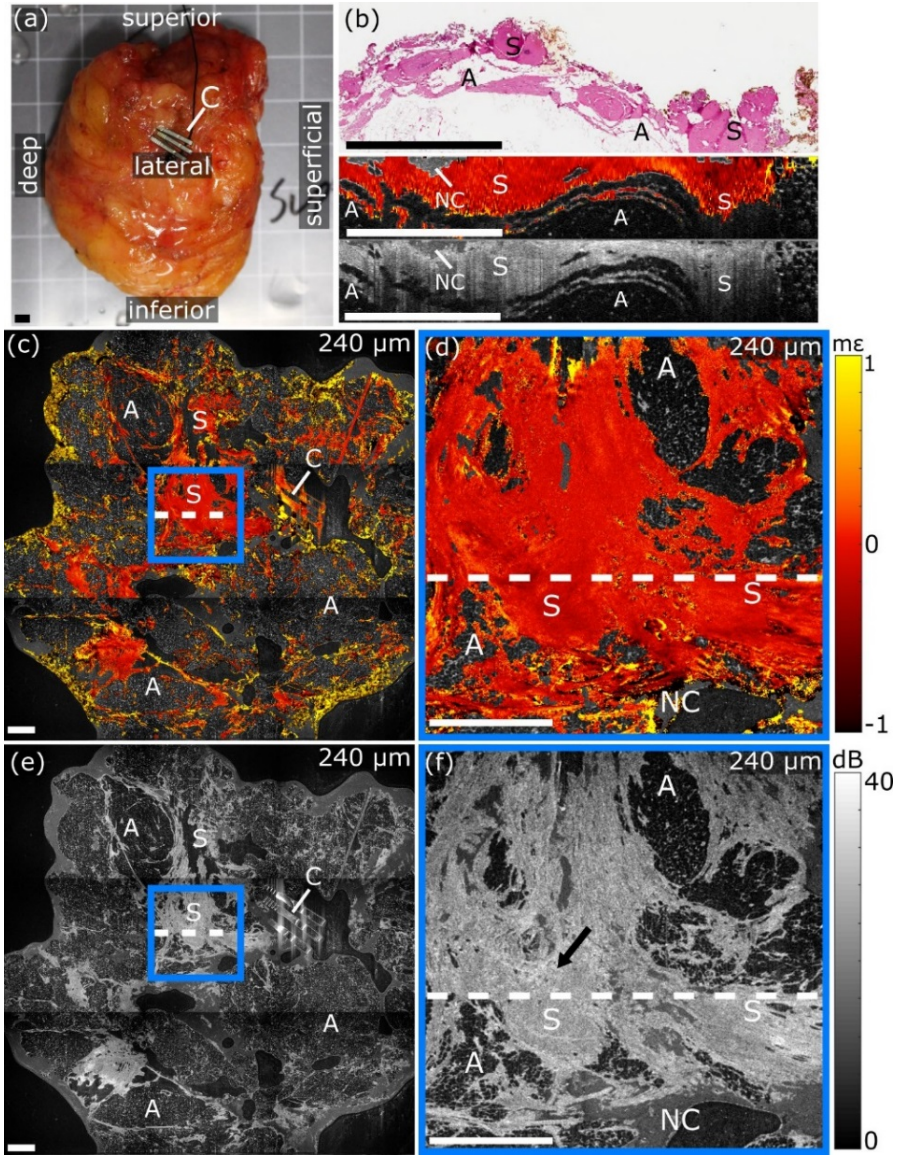

Fig. 3. OCME of the lateral margin of freshly excised WLE specimen demonstrating contrast in uninvolved stroma (see Visualization 2). (a) Photograph of the lateral margin. (b) Digital micrograph and co-registered B-scans. (c) Wide-field and (d) magnified *en face* micro-elastogram. (e) Wide-field and (f) magnified *en face* OCT image. The arrow in (f) indicates an area of heterogeneous OCT intensity. *En face* images are presented at a depth of 240 µm. The white dashed lines in (c)-(f) indicate the location of the digital micrograph. All scale bars 3 mm. A, Adipose tissue; C, Clips; NC, Non-contact; S, Uninvolved stroma.

In Fig. 4, we present images of a deep margin involved with invasive ductal carcinoma, excised from a 65-year-old patient. A photograph of the margin, which measured 35 × 38 mm, is shown in Fig. 4(a). Three clips, (C), attached to the suture from the lateral margin are visible in the photograph. The digital micrograph, Fig. 4(b), reveals that the deep margin was involved by highly cellular invasive ductal carcinoma (IDC), detected 260 µm from the inked surface of the specimen. The digital micrograph also shows the specimen comprised adipose tissue (A) and stroma (S). Co-registered B-scans are presented in Fig. 4(b). The location of the digital micrograph is indicated by white dashed lines in the *en face* images

Biomedical Optics EXPRESS

shown in Fig. 4(c)- 4(f). The wide-field micro-elastogram, Fig. 4(c), and OCT image, Fig. 4(e), show that the tissue comprises adipose and dense tissue. The dense tissue to the right of the clips appears organized in structure in the wide-field micro-elastogram, with bands running in parallel, indicative of mature fibrous tissue [31]. Much of the dense tissue in this specimen transitions to adipose deeper within the specimen, however, the magnified micro-elastogram, Fig. 4(d), shows a region of dense tissue that grows in size with depth. This region of dense tissue can also be seen in Visualization 3 and the B-scans in Fig. 4(b). The dense tissue in this region exhibits disorganized heterogeneous strain, in both the *en face* and B-scan plane, indicative of invasive ductal carcinoma [30,43]. It is interesting to note that the central area of this tumor, *i.e.*, the tumor away from the margin, contains more intervening stroma and would likely exhibit more clearly defined strain heterogeneity if this tissue had been dissected to expose the dense center for imaging, as in the case of mastectomies [34]. The wide-field *en face* OCT image, Fig. 4(e), highlights the organized structure and directionality of the fibrous tissue to the right of the clips.

The magnified OCT image highlights a limitation of the segmentation algorithm. Due to the coherence gate curvature (CG) there is a step change in OCT intensity where two sub-images are stitched together, visible in Fig. 4(f). This has resulted in the algorithm incorrectly identifying dense tissue as non-dense tissue, manifesting as a vertical discontinuity in the magnified micro-elastogram in Fig. 4(d). This specimen demonstrates a key difference in tumor architecture between WLE and mastectomy specimens as only the leading edge of the tumor is present in the margin. We expect this will prove to be a common trait for WLE specimens, as, often, the bulk of the tumor will be located near the center of the specimen, and only the leading edges of the tumor mass will be imaged. In comparison, in the previous benign case, Visualization 2, much of the dense tissue transitioned to adipose at increasing depths in the specimen. This case also highlights how the complementary contrast provided by OCME and OCT aids in the identification of tumor.

In Fig. 5, we present images of the superficial margin of the WLE specimen presented in Fig. 3. The superficial margin of this specimen was involved by mucinous carcinoma. A photograph of the margin, which measured ~65 × 60 mm, is presented in Fig. 5(a). The digital micrograph, Fig. 5(b), shows the distinctive micro-architecture of mucinous carcinoma (MC), *i.e.*, cancer cells suspended in pools of mucin. Similar to the previous case, only the leading edge of the mucinous carcinoma is present at the surgical margin. Co-registered B-scans are presented in Fig. 5(b). The location of the digital micrograph in *en face* images is indicated by white dashed lines in Fig. 5(c)-5(f). In this case, the OCT images more clearly delineate the mucinous carcinoma from adipose tissue compared to the micro-elastograms. In the wide-field OCT image, Fig. 5(e), the specimen appears to comprise mainly adipose tissue (A), with some thin strands of connective stroma (S). A region of mucinous carcinoma is presented in the magnified OCT image (Fig. 5(f)). The mucin manifests as more uniformly scattering than the surrounding adipose tissue, with the tumor cells appearing as dots of high OCT intensity [44]. In the wide-field micro-elastogram, Fig. 5(c), the strain in the connective tissue appears uniform, indicative of uninvolved stroma. The magnified micro-elastogram, Fig. 5(d), shows that the automated segmentation algorithm identified the mucinous carcinoma. Much of the strain in this region is positive, *i.e.*, moving towards the imaging window during compression, which may indicate that the surrounding tissue is displacing mucin. The arrows in the low-magnification images, Fig. 5(d) and 5(f), point to a region where the mucinous carcinoma appears closer to the margin than in the digital micrograph, highlighting that the spatial sampling (~3–7 mm) during tissue sectioning can be a limiting factor when performing the standard histopathological analysis of WLE specimens. A potential advantage of OCT-based imaging techniques is the ability to more fully assess the surface of these specimens through visualization of *en face* images.

Biomedical Optics EXPRESS

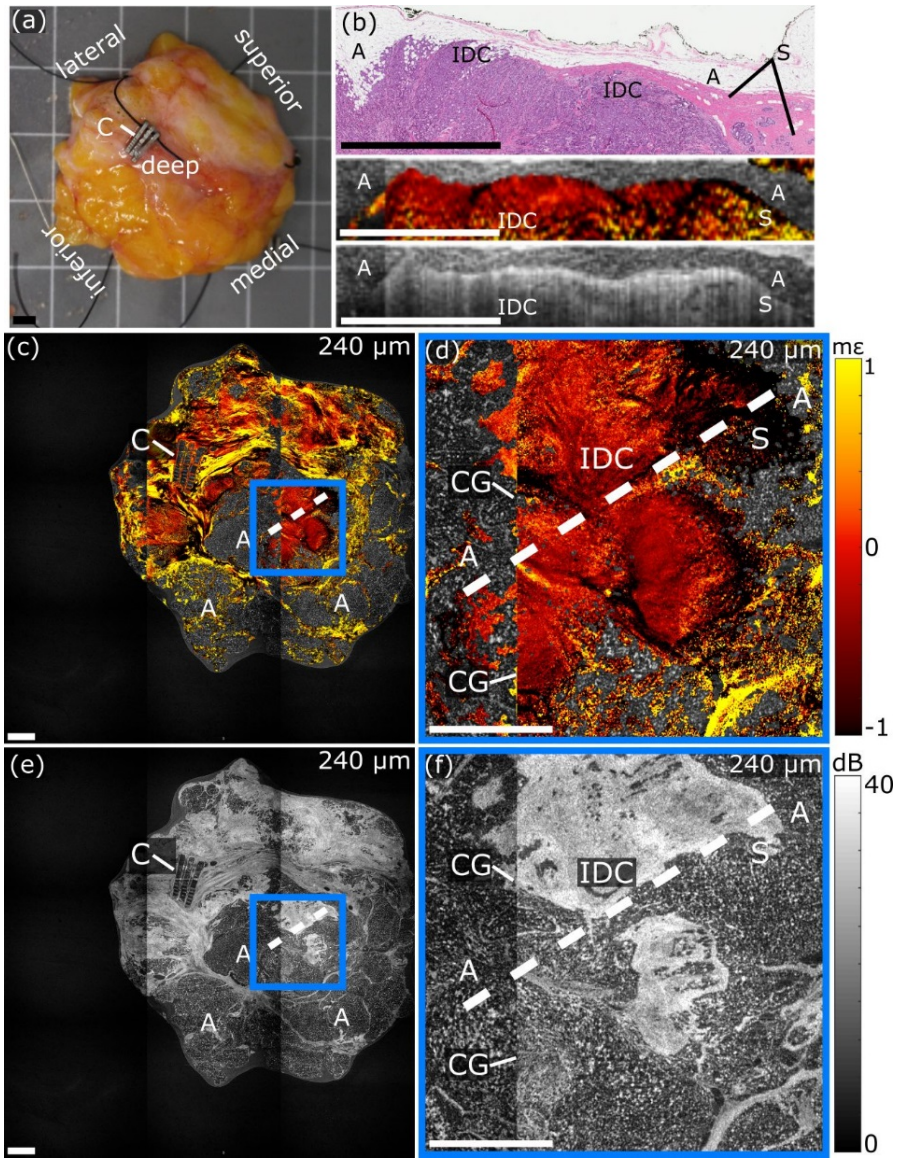

Fig. 4. OCME of the deep margin of a freshly excised WLE specimen demonstrating contrast in highly cellular invasive ductal carcinoma (see Visualization 3). (a) Photograph of the deep margin. (b) Digital micrograph and co-registered B-scans. (c) Wide-field and (d) magnified *en face* micro-elastogram. (e) Wide-field and (f) magnified *en face* OCT image. *En face* images are presented at a depth of 240 µm. The white dashed lines in (c)-(f) indicate the location of the digital micrograph. All scale bars 3 mm. A, Adipose tissue; C, Clip; CG, Coherence gate curvature artifact; IDC, Invasive ductal carcinoma; S, Stroma

Biomedical Optics EXPRESS

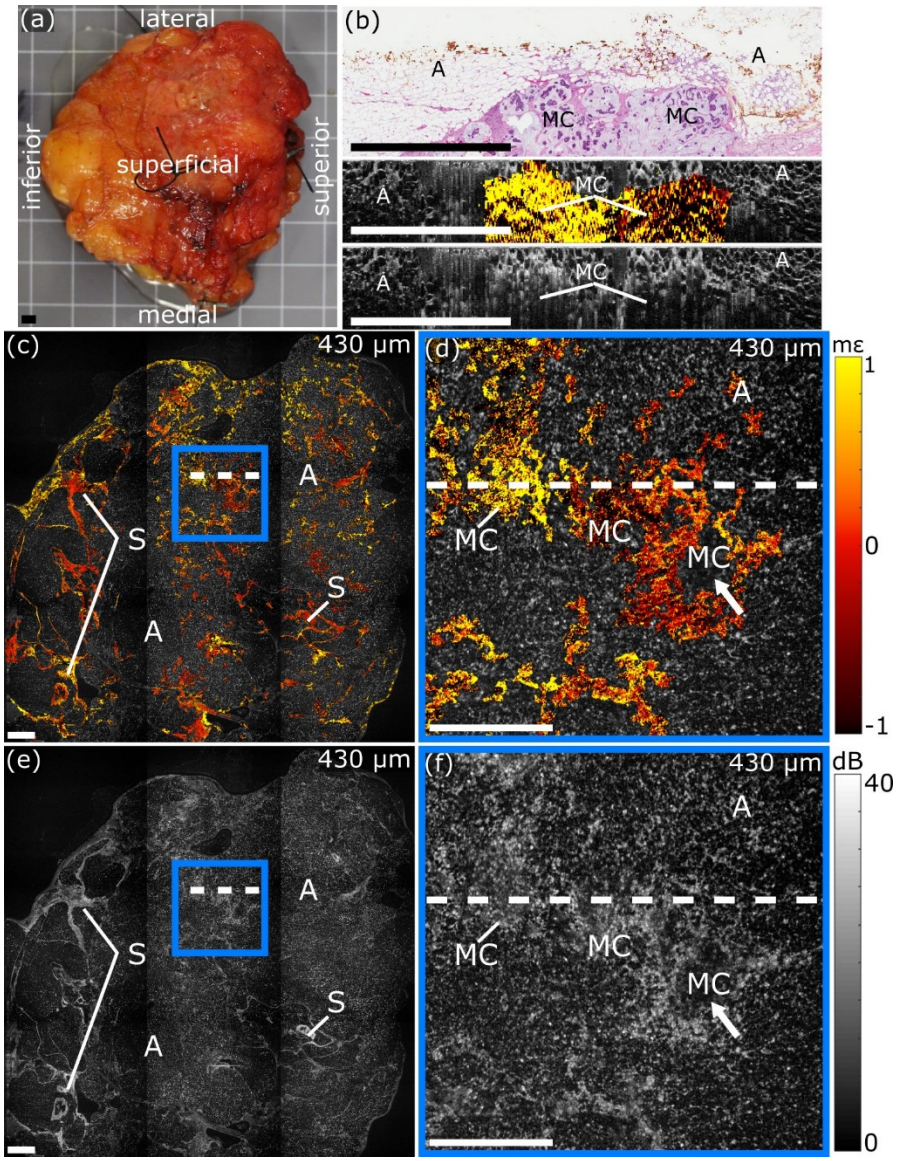

Fig. 5. OCME of the superficial margin of a freshly excised WLE specimen demonstrating contrast in mucinous carcinoma (see Visualization 4). (a) Photograph of the superficial margin. (b) Digital micrograph and co-registered B-scans. (c) Wide-field and (d) magnified *en face* micro-elastogram. (e) Wide-field and (f) magnified *en face* OCT image. *En face* images are presented at a depth of 430 µm. The white dashed lines in (c)-(f) indicate the location of the digital micrograph. All scale bars 3 mm. A, Adipose tissue; MC, Mucinous carcinoma; S, Stroma.

In Fig. 6, we present images of an involved superior margin containing solid-papillary carcinoma, excised from a 69-year-old patient. A photograph of the margin, which measured ~35 × 60 mm, is shown in Fig. 6(a). The digital micrograph, Fig. 6(b), shows that the superior margin was involved by solid-papillary carcinoma (PC) and also contained regions of adipose tissue (A). Co-registered B-scans are presented in Fig. 6(b). The location of the digital micrograph in *en face* images is indicated by white dashed lines in Fig. 6(c)-6(f).

Biomedical Optics EXPRESS

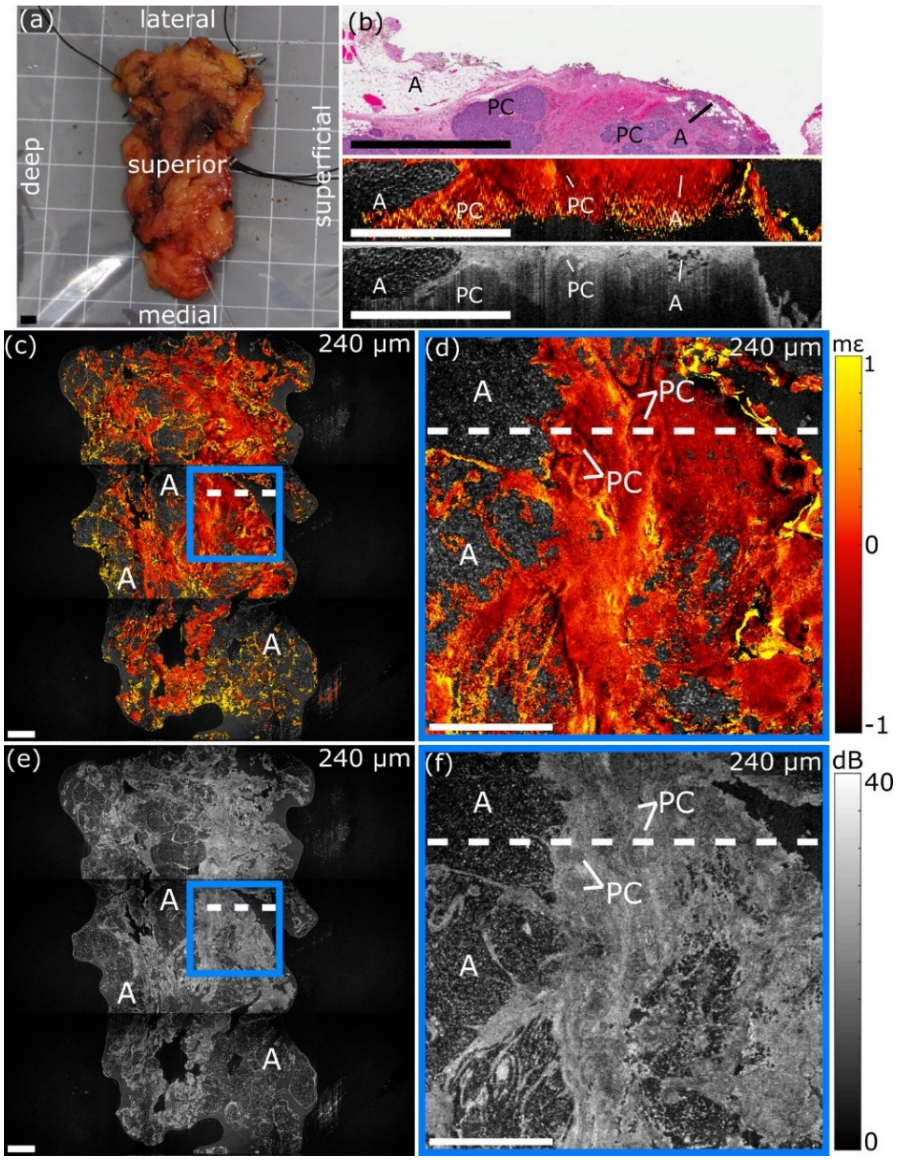

Fig. 6. OCME of the superior margin of a freshly excised WLE specimen demonstrating contrast in solid-papillary carcinoma (see Visualization 5). (a) Photograph of the superior margin. (b) Digital micrograph and co-registered B-scans. (c) Wide-field and (d) magnified *en face* micro-elastogram. (e) Wide-field and (f) magnified *en face* OCT image. *En face* images are presented at a depth of 240 µm. The white dashed lines in (c)-(f) indicate the location of the digital micrograph. All scale bars 3 mm. A, Adipose tissue; PC, Solid-papillary carcinoma.

The wide-field micro-elastogram, Fig. 6(c), and OCT image, Fig. 6(e), show that the specimen comprises large regions of dense tissue intermingled with adipose tissue. The bulk of the specimen exhibits relatively homogeneous strain in the wide-field micro-elastogram, with the exception of boundary effects where the stroma is infiltrated by adipose tissue, which can manifest as strain heterogeneity, as highlighted in Table 1. The magnified micro-elastogram, Fig. 6(d), delineates the boundaries of the solid-papillary carcinoma (PC), manifesting as luminal features highlighted with compressive (negative) strain. The boundaries of the solid-papillary carcinoma are also visible in the micro-elastogram B-scan (Fig. 6(b)). While such luminal features are also present in ducts, the diameter, >1 mm, of the

Biomedical Optics EXPRESS

solid-papillary carcinoma nodules are larger than expected in normal ducts Also, unlike a typical duct, the papillary carcinoma does not form a tubular structure and appears more nodular in shape when visualized in 3D (Visualization 5). The magnified OCT image, Fig. 6(f), shows the region containing the solid-papillary carcinoma; however, the OCT contrast is subtle in comparison to the micro-elastogram.

4. Discussion

In this study, we performed OCME on 28 margins from 17 WLE specimens excised from patients undergoing breast-conserving surgery. We have demonstrated the clinical feasibility of performing OCME on intact WLE specimens, and have presented developments that enable automated generation of fused *en face* micro-elastograms and co-registration of WLE histology to validate contrast. A summary of the observations of common tissue types present in the margins imaged during the study was presented in Table 1. The representative micro-elastograms and OCT images presented here demonstrate mechanical contrast observed in mastectomy specimens is retained for a range of tissue types in WLE specimens. The results also demonstrate that the complementary contrast present in micro-elastograms and OCT images aids in the visualization of a range of features in freshly excised human breast tissue.

In addition to the changes in micro-architecture and geometry already highlighted in this manuscript, there are some further challenges to overcome in transitioning OCME from mastectomy specimens to the clinical scenario of imaging the surgical margin of WLE specimens. For example, WLE specimens occasionally sustain thermal damage during excision, caused by the use of electrosurgical instruments to excise the tissue and coagulate severed blood vessels. Thermal damage was identified by the pathologist during annotation of the digital micrographs. We observed, in some cases, that excessive thermal damage results in regions of non-contact, as the specimen does not readily deform to contact the imaging window fully. Non-contact can result in strain heterogeneity with a similar spatial frequency as invasive tumor [30,34]. In a related technique, quantitative micro-elastography, a thin compliant layer is placed between the imaging window and the specimen to measure tissue elasticity [34,45]. An advantage of the layer is that it deforms under preload to accommodate the rough surface of the specimen, resulting in more uniform contact and reducing strain heterogeneity arising from the boundary conditions [34]. In ongoing work investigating quantitative micro-elastography, we have acquired images of over 140 margins. From these, excessive thermal damage from electrosurgical instruments appears to sometimes result in elevated tissue stiffness, but in the majority of the cases, this effect has not been significant enough to cause benign tissue to be confused with tumor.

Additionally, in previous studies on mastectomy specimens, quantitative micro-elastography has demonstrated the ability to detect a range of tumors by presenting micro-elastograms of elasticity alongside strain. In particular, quantitative micro-elastography has proven beneficial in detecting highly cellular invasive tumors with little intervening stroma that present as subtle strain heterogeneity, as is the case in Fig. 4 [34]. A further advantage of incorporating a compliant layer is that the interface between the imaging window and the compliant layer acts as the reference reflection; ensuring that the intensity of the reference reflection is constant across the entire field-of-view. By comparison, in OCME, the refractive index of the tissue in contact with the imaging window may vary, resulting in a change in the intensity of the reference reflection. A recent study has demonstrated the ability of quantitative micro-elastography to image a wide-field-of-view [34], in future work will continue to explore the extension of quantitative micro-elastography for imaging of WLE specimens.

This study incorporates the use of an automated masking algorithm to segment regions of dense tissue from regions of non-dense tissue, *e.g.*, adipose or non-contact. The algorithm allows for 3D stacks of *en face* micro-elastograms to be processed for analysis without manual intervention. However, the robustness of the masking algorithm depends on the

Biomedical Optics EXPRESS

quality of the experimental setup. For example, variations in OCT intensity caused by coherence gate curvature results in a step change in OCT intensity in the mosaicked wide-field images, apparent in Fig. 4(d) and Visualization 2 (below 400 μm), which cause misclassification of tissues. Although this effect is difficult to eliminate by physically adjusting the imaging equipment, it may be possible to reduce it through image processing, for example, by using a calibration image [46]. Alternatively, region-growing techniques may be implemented to combat this issue [47]. Additionally, regions of non-dense tissue with high optical backscattering may be erroneously classified as dense tissue. An example of this is seen in the clips (C) in Fig. 3(c) and the high OCT intensity present in this adipose tissue (A) in Fig. 4(d). Preliminary work explored the use of an algorithm based on texture classification, which would be less likely to misclassify adipose regions. However, the algorithm possessed lower resolution compared to the binary masking algorithm used here.

The scanning protocol presented here allows us to scan a maximum of 2 margins within ~30 minutes. To enable scanning of all margins, we need to improve the scanning protocol to reduce the scanning time. Faster scanning could be achieved in a number of ways, for example, by performing depth-encoded OCME to simultaneously acquire two 3D OCME data sets from opposite sides of the specimen [48] or by utilizing a Fourier-domain mode-locked swept-source laser which has demonstrated phase-sensitive optical coherence elastography with an A-scan frequency of ~1.5 MHz [49]. Improvements in the post-processing speed also need to be made for eventual intraoperative deployment. Post-processing of data sets, including segmentation and image generation, took ~3 hours per margin and was performed in the days following data acquisition in this feasibility study. For eventual intraoperative deployment of OCME, this must be reduced. Near video-rate OCME processing has previously been demonstrated using a commercial-grade graphics processing unit [50]. Incorporating such a graphics processing unit in the current system has the potential to provide intraoperative feedback in a surgical setting.

The methods described in this manuscript enable co-registration of histology, processed and documented following standard clinical workflows, with wide-field *en face* images. While the method can compensate for tissue shrinkage that occurs during chemical fixation, it assumes that the tissue shrinks uniformly in all directions. However, tissue often distorts during fixation. By identifying bulk features, such as regions of adipose tissue or fibrous tissue and features in the surface topology in the low-resolution OCT volume, this method has proven robust in the co-registration of digital micrographs with *en face* images and the validation of contrast in the results presented in this study.

5. Conclusion

In this manuscript, we have presented a study investigating the clinical feasibility of OCME for imaging tumor margins performed on specimens excised during breast-conserving surgery. We have outlined the challenges in translating OCME from mastectomy specimens to the more clinically relevant WLE specimens. The images presented here demonstrate that the complementary contrast in micro-elastograms and OCT images aids in visualizing a range of features in human breast tissue. We have described an algorithm to segment dense and non-dense tissue regions in OCT images, which is required for the rapid generation of fused micro-elastograms. We have also presented a method to co-register histology from WLE specimens with wide-field *en face* micro-elastograms and OCT images. The techniques developed to demonstrate the suitability of OCME for imaging tumor margins for a large set of specimens. This study will provide a framework for a more extensive study determining the diagnostic accuracy of OCME for tumor margin assessment in breast-conserving surgery.

Biomedical Optics EXPRESS

Funding

Australian Research Council; the Department of Health, Western Australia; Cancer Council, Western Australia; OncoRes Medical; William and Marlene Schrader Trust of The University of Western Australia.

Acknowledgments

The authors acknowledge Dr. Andrea Curatolo, Mr. Rowan Sanderson and Ms. Lucinda Watts for assisting with the clinical aspects of this project. We also thank Dr. Philip Wijesinghe for fruitful discussions regarding colormaps. The authors acknowledge the facilities, and the scientific and technical assistance of the Australian Microscopy & Microanalysis Research Facility at the Centre for Microscopy, Characterization & Analysis, The University of Western Australia, a facility funded by the University, State and Commonwealth Governments.

Disclosures

BFK: OncoRes Medical (F, I), KMK, LC, BL, and CMS: OncoRes Medical (I). The other authors declare that there are no conflicts of interest related to this article.

References

1. "Breast cancer facts & figures 2017-2018" (American Cancer Society, 2017), retrieved March 2018, *https://www.cancer.org/content/dam/cancer-org/research/cancer-facts-and-statistics/breast-cancer-facts-and-figures/breast-cancer-facts-and-figures-2017-2018.pdf*.
2. H. Ballal, D. B. Taylor, A. G. Bourke, B. Latham, and C. M. Saunders, "Predictors of re-excision in wire-guided wide local excision for early breast cancer: a Western Australian multi-centre experience," ANZ J. Surg. **85**(7-8), 540–545 (2015).
3. R. Jeevan, D. A. Cromwell, M. Trivella, G. Lawrence, O. Kearins, J. Pereira, C. Sheppard, C. M. Caddy, and J. H. P. van der Meulen, "Reoperation rates after breast conserving surgery for breast cancer among women in England: retrospective study of hospital episode statistics," BMJ **345**(7), e4505 (2012).
4. E. D. Kurniawan, M. H. Wong, I. Windle, A. Rose, A. Mou, M. Buchanan, J. P. Collins, J. A. Miller, R. L. Gruen, and G. B. Mann, "Predictors of surgical margin status in breast-conserving surgery within a breast screening program," Ann. Surg. Oncol. **15**(9), 2542–2549 (2008).
5. B. J. Adams, C. K. Zoon, C. Stevenson, P. Chitnavis, L. Wolfe, and H. D. Bear, "The role of margin status and reexcision in local recurrence following breast conservation surgery," Ann. Surg. Oncol. **20**(7), 2250–2255 (2013).
6. L. Jacobs, "Positive margins: The challenge continues for breast surgeons," Ann. Surg. Oncol. **15**(5), 1271–1272 (2008).
7. I. Gage, S. J. Schnitt, A. J. Nixon, B. Silver, A. Recht, S. L. Troyan, T. Eberlein, S. M. Love, R. Gelman, J. R. Harris, and J. L. Connolly, "Pathologic margin involvement and the risk of recurrence in patients treated with breast-conserving therapy," Cancer **78**(9), 1921–1928 (1996).
8. E. R. St John, R. Al-Khudairi, H. Ashrafian, T. Athanasiou, Z. Takats, D. J. Hadjiminas, A. Darzi, and D. R. Leff, "Diagnostic accuracy of intraoperative techniques for margin assessment in breast cancer surgery: a meta-analysis," Ann. Surg. **265**(2), 300–310 (2017).
9. K. Esbona, Z. Li, and L. G. Wilke, "Intraoperative imprint cytology and frozen section pathology for margin assessment in breast conservation surgery: a systematic review," Ann. Surg. Oncol. **19**(10), 3236–3245 (2012).
10. J. M. Jorns, D. Visscher, M. Sabel, T. Breslin, P. Healy, S. Daignaut, J. L. Myers, and A. J. Wu, "Intraoperative Frozen Section Analysis of Margins in Breast Conserving Surgery Significantly Decreases Reoperative Rates: One-Year Experience at an Ambulatory Surgical Center," Am. J. Clin. Pathol. **138**(5), 657–669 (2012).
11. R. Laucirica, "Intraoperative Assessment of the Breast: Guidelines and Potential Pitfalls," Arch. Pathol. Lab. Med. **129**(12), 1565–1574 (2005).
12. E. F. Brachtel, N. B. Johnson, A. E. Huck, T. L. Rice-Stitt, M. G. Vangel, B. L. Smith, G. J. Tearney, and D. Kang, "Spectrally encoded confocal microscopy for diagnosing breast cancer in excision and margin specimens," Lab. Invest. **96**(4), 459–467 (2016).
13. S. J. Erickson-Bhatt, R. M. Nolan, N. D. Shemonski, S. G. Adie, J. Putney, D. Darga, D. T. McCormick, A. J. Cittadine, A. M. Zysk, M. Marjanovic, E. J. Chaney, G. L. Monroy, F. A. South, K. A. Cradock, Z. G. Liu, M. Sundaram, P. S. Ray, and S. A. Boppart, "Real-time imaging of the resection bed using a handheld probe to reduce incidence of microscopic positive margins in cancer surgery," Cancer Res. **75**(18), 3706–3712 (2015).
14. A. K. Glaser, N. P. Reder, Y. Chen, E. F. McCarty, C. Yin, L. Wei, Y. Wang, L. D. True, and J. T. C. Liu, "Light-sheet microscopy for slide-free non-destructive pathology of large clinical specimens," Nat. Biomed. Eng. **1**(7), 0084 (2017).

Biomedical Optics EXPRESS

15. P. Gao, B. Han, Y. Du, G. Zhao, Z. Yu, W. Xu, C. Zheng, and Z. Fan, "The clinical application of Raman spectroscopy for breast cancer detection," J. Spectrosc. **2017**, 5383948 (2017).
16. F. T. Nguyen, A. M. Zysk, E. J. Chaney, J. G. Kotynek, U. J. Oliphant, F. J. Bellafiore, K. M. Rowland, P. A. Johnson, and S. A. Boppart, "Intraoperative evaluation of breast tumor margins with optical coherence tomography," Cancer Res. **69**(22), 8790–8796 (2009).
17. J. Zhang, J. Rector, J. Q. Lin, J. H. Young, M. Sans, N. Katta, N. Giese, W. Yu, C. Nagi, J. Suliburk, J. Liu, A. Bensussan, R. J. DeHoog, K. Y. Garza, B. Ludolph, A. G. Sorace, A. Syed, A. Zahedivash, T. E. Milner, and L. S. Eberlin, "Nondestructive tissue analysis for *ex vivo* and *in vivo* cancer diagnosis using a handheld mass spectrometry system," Sci. Transl. Med. **9**(406), eaan3968 (2017).
18. G. Thomas, T. Q. Nguyen, I. J. Pence, B. Caldwell, M. E. O'Connor, J. Giltnane, M. E. Sanders, A. Grau, I. Meszoely, M. Hooks, M. C. Kelley, and A. Mahadevan-Jansen, "Evaluating feasibility of an automated 3-dimensional scanner using Raman spectroscopy for intraoperative breast margin assessment," Sci. Rep. **7**(1), 13548 (2017).
19. S. Abeytunge, B. Larson, G. Peterson, M. Morrow, M. Rajadhyaksha, and M. P. Murray, "Evaluation of breast tissue with confocal strip-mosaicking microscopy: a test approach emulating pathology-like examination," J. Biomed. Opt. **22**(3), 034002 (2017).
20. L. C. Cahill, M. G. Giacomelli, T. Yoshitake, H. Vardeh, B. E. Faulkner-Jones, J. L. Connolly, C.-K. Sun, and J. G. Fujimoto, "Rapid virtual hematoxylin and eosin histology of breast tissue specimens using a compact fluorescence nonlinear microscope," Lab. Invest. **98**(1), 150–160 (2018).
21. M. G. Giacomelli, T. Yoshitake, L. C. Cahill, H. Vardeh, L. M. Quintana, B. E. Faulkner-Jones, J. Brooker, J. L. Connolly, and J. G. Fujimoto, "Multiscale nonlinear microscopy and widefield white light imaging enables rapid histological imaging of surgical specimen margins," Biomed. Opt. Express **9**(5), 2457–2475 (2018).
22. A. M. Zysk, K. Chen, E. Gabrielson, L. Tafra, E. A. May Gonzalez, J. K. Canner, E. B. Schneider, A. J. Cittadine, P. Scott Carney, S. A. Boppart, K. Tsuchiya, K. Sawyer, and L. K. Jacobs, "Intraoperative assessment of final margins with a handheld optical imaging probe during breast-conserving surgery may reduce the reoperation rate: Results of a multicenter study," Ann. Surg. Oncol. **22**(10), 3356–3362 (2015).
23. R. Ha, L. C. Friedlander, H. Hibshoosh, C. Hendon, S. Feldman, S. Ahn, H. Schmidt, M. K. Akens, M. Fitzmaurice, B. C. Wilson, and V. L. Mango, "Optical coherence tomography: A novel imaging method for post-lumpectomy breast margin assessment—A multi-reader study," Acad. Radiol. **25**(3), 279–287 (2018).
24. M. J. Whitley, D. M. Cardona, A. L. Lazarides, I. Spasojevic, J. M. Ferrer, J. Cahill, C.-L. Lee, M. Snuderl, D. G. Blazer 3rd, E. S. Hwang, R. A. Greenup, P. J. Mosca, J. K. Mito, K. C. Cuneo, N. A. Larrier, E. K. O'Reilly, R. F. Riedel, W. C. Eward, D. B. Strasfeld, D. Fukumura, R. K. Jain, W. D. Lee, L. G. Griffith, M. G. Bawendi, D. G. Kirsch, and B. E. Brigman, "A mouse-human phase 1 co-clinical trial of a protease-activated fluorescent probe for imaging cancer," Sci. Transl. Med. **8**(320), 320ra4 (2016).
25. M. R. Grootendorst, M. Cariati, S. E. Pinder, A. Kothari, M. Douek, T. Kovacs, H. Hamed, A. Pawa, F. Nimmo, J. Owen, V. Ramalingam, S. Sethi, S. Mistry, K. Vyas, D. S. Tuch, A. Britten, M. Van Hemelrijck, G. J. Cook, C. Sibley-Allen, S. Allen, and A. Purushotham, "Intraoperative Assessment of Tumor Resection Margins in Breast-Conserving Surgery Using ^{18}F-FDG Cerenkov Luminescence Imaging: A First-in-Human Feasibility Study," J. Nucl. Med. **58**(6), 891–898 (2017).
26. S. A. Boppart, J. Q. Brown, C. S. Farah, E. Kho, L. Marcu, C. M. Saunders, and H. J. C. M. Sterenborg, "Label-free optical imaging technologies for rapid translation and use during intraoperative surgical and tumor margin assessment," in (SPIE, 2017), 10.
27. B. F. Kennedy, K. M. Kennedy, and D. D. Sampson, "A review of optical coherence elastography: fundamentals, techniques and prospects," IEEE J. Sel. Top. Quantum Electron. **20**(2), 272 (2014).
28. B. F. Kennedy, P. Wijesinghe, and D. D. Sampson, "The emergence of optical elastography in biomedicine," Nat. Photonics **11**(4), 215–221 (2017).
29. B. F. Kennedy, R. A. McLaughlin, K. M. Kennedy, L. Chin, A. Curatolo, A. Tien, B. Latham, C. M. Saunders, and D. D. Sampson, "Optical coherence micro-elastography: mechanical-contrast imaging of tissue microstructure," Biomed. Opt. Express **5**(7), 2113–2124 (2014).
30. B. F. Kennedy, R. A. McLaughlin, K. M. Kennedy, L. Chin, P. Wijesinghe, A. Curatolo, A. Tien, M. Ronald, B. Latham, C. M. Saunders, and D. D. Sampson, "Investigation of optical coherence micro-elastography as a method to visualize cancers in human breast tissue," Cancer Res. **75**(16), 3236–3245 (2015).
31. W. M. Allen, L. Chin, P. Wijesinghe, R. W. Kirk, B. Latham, D. D. Sampson, C. M. Saunders, and B. F. Kennedy, "Wide-field optical coherence micro-elastography for intraoperative assessment of human breast cancer margins," Biomed. Opt. Express **7**(10), 4139–4153 (2016).
32. B. F. Kennedy, S. H. Koh, R. A. McLaughlin, K. M. Kennedy, P. R. T. Munro, and D. D. Sampson, "Strain estimation in phase-sensitive optical coherence elastography," Biomed. Opt. Express **3**(8), 1865–1879 (2012).
33. L. Scolaro, R. A. McLaughlin, B. F. Kennedy, C. M. Saunders, and D. D. Sampson, "A review of optical coherence tomography in breast cancer," Photonics Lasers Med. **3**(3), 225–240 (2014).
34. W. M. Allen, K. M. Kennedy, Q. Fang, L. Chin, A. Curatolo, L. Watts, R. Zilkens, S. L. Chin, B. F. Dessauvagie, B. Latham, C. M. Saunders, and B. F. Kennedy, "Wide-field quantitative micro-elastography of human breast tissue," Biomed. Opt. Express **9**(3), 1082–1096 (2018).
35. L. Chin, A. Curatolo, B. F. Kennedy, B. J. Doyle, P. R. T. Munro, R. A. McLaughlin, and D. D. Sampson, "Analysis of image formation in optical coherence elastography using a multiphysics approach," Biomed. Opt. Express **5**(9), 2913–2930 (2014).

Biomedical Optics EXPRESS

36. A. C. Chan, E. Y. Lam, and V. J. Srinivasan, "Comparison of Kasai autocorrelation and maximum likelihood estimators for Doppler optical coherence tomography," IEEE Trans. Med. Imaging **32**(6), 1033–1042 (2013).
37. "MATLAB and Octave Functions for Computer Vision and Image Processing." (Kovesi, Peter, 2000), retrieved April 2018, *http://www.peterkovesi.com/matlabfns/*.
38. P. Perona and J. Malik, "Scale-space and edge detection using anisotropic diffusion," IEEE Trans. Pattern Anal. Mach. Intell. **12**(7), 629–639 (1990).
39. J. C. Russ and F. B. Neal, *The Image Processing Handbook, Seventh Edition* (CRC Press, 2017).
40. N. Otsu, "A Threshold Selection Method from Gray-Level Histograms," IEEE Trans. Syst. Man Cybern. **9**(1), 62–66 (1979).
41. J. Schindelin, I. Arganda-Carreras, E. Frise, V. Kaynig, M. Longair, T. Pietzsch, S. Preibisch, C. Rueden, S. Saalfeld, B. Schmid, J. Y. Tinevez, D. J. White, V. Hartenstein, K. Eliceiri, P. Tomancak, and A. Cardona, "Fiji: an open-source platform for biological-image analysis," Nat. Methods **9**(7), 676–682 (2012).
42. M. Thill, "MarginProbe: intraoperative margin assessment during breast conserving surgery by using radiofrequency spectroscopy," Expert Rev. Med. Devices **10**(3), 301–315 (2013).
43. L. Chin, B. Latham, C. M. Saunders, D. D. Sampson, and B. F. Kennedy, "Simplifying the assessment of human breast cancer by mapping a micro-scale heterogeneity index in optical coherence elastography," J. Biophotonics **10**(5), 690–700 (2017).
44. C. Zhou, D. W. Cohen, Y. Wang, H.-C. Lee, A. E. Mondelblatt, T.-H. Tsai, A. D. Aguirre, J. G. Fujimoto, and J. L. Connolly, "Integrated optical coherence tomography and microscopy for *ex vivo* multiscale evaluation of human breast tissues," Cancer Res. **70**(24), 10071–10079 (2010).
45. K. M. Kennedy, L. Chin, R. A. McLaughlin, B. Latham, C. M. Saunders, D. D. Sampson, and B. F. Kennedy, "Quantitative micro-elastography: imaging of tissue elasticity using compression optical coherence elastography," Sci. Rep. **5**(1), 15538 (2015).
46. B. W. Graf, S. G. Adie, and S. A. Boppart, "Correction of coherence gate curvature in high numerical aperture optical coherence imaging," Opt. Lett. **35**(18), 3120–3122 (2010).
47. F. Gasca, L. Ramrath, G. Huettmann, and A. Schweikard, "Automated segmentation of tissue structures in optical coherence tomography data," J. Biomed. Opt. **14**(3), 034046 (2009).
48. Q. Fang, L. Frewer, P. Wijesinghe, W. M. Allen, L. Chin, J. Hamzah, D. D. Sampson, A. Curatolo, and B. F. Kennedy, "Depth-encoded optical coherence elastography for simultaneous volumetric imaging of two tissue faces," Opt. Lett. **42**(7), 1233–1236 (2017).
49. M. Singh, C. Wu, C.-H. Liu, J. Li, A. Schill, A. Nair, and K. V. Larin, "Phase-sensitive optical coherence elastography at 1.5 million A-Lines per second," Opt. Lett. **40**(11), 2588–2591 (2015).
50. R. W. Kirk, B. F. Kennedy, D. D. Sampson, and R. A. McLaughlin, "Near video-rate optical coherence elastography by acceleration with a graphics processing unit," J. Lightwave Technol. **33**(16), 3481–3485 (2015).